01 Jan 2021

Thermal Mapping of Metal Casting Mold using High Resolution Distributed Fiber-Optic Sensors

Muhammad Roman

Damilola Balogun

Chen Zhu
Missouri University of Science and Technology, cznwq@mst.edu

Laura Bartlett
Missouri University of Science and Technology, lnmkvf@mst.edu

et. al. For a complete list of authors, see https://scholarsmine.mst.edu/psmrc_facwork/32

Thermal Mapping of Metal Casting Mold Using High-Resolution Distributed Fiber-Optic Sensors

Muhammad Roman, *Graduate Student Member, IEEE*, Damilola Balogun, Chen Zhu, *Member, IEEE*, Laura Bartlett, Ronald J. O'Malley, Rex E. Gerald II, and Jie Huang, *Senior Member, IEEE*

***Abstract*— This article reports a technique to embed optical fiber into a copper mold plate for generating high-density thermal maps of the mold during the process of metal casting. The temperature measurements were based on acquiring and interpreting Rayleigh backscattering (RBS) signals from embedded fiber, using the interrogation technique of optical frequency domain reflectometry (OFDR). The instrumented mold plate was used to perform a cast-iron dip test and a steel dip test in a 200 lb induction furnace. The maximum temperatures recorded by the embedded fiber-optic sensors were 469 °C and 388 °C in the cast-iron and steel dip tests, respectively. The closely spaced and rapidly fluctuating temperature features that were imparted to the mold wall during solidification were successfully mapped with a high spatial resolution (0.65 mm) and a fast measurement rate (25 Hz) using a commercial OFDR interrogator (LUNA ODiSI 6108). Moreover, the thickness of the solidified steel shell was measured, and a thickness map of the shell was generated. A good correlation was observed between the thickness of the solidified shell and the temperature of the mold, as regions with higher and lower temperatures in the thermal profile of the mold corresponded to thicker and thinner areas on the shell, respectively. The dip testing experiments demonstrate that RBS-based fiber-optic sensing is a feasible and effective method for generating information-rich thermal maps of caster molds. The information obtained from thermal maps can be useful for improving the quality of the metal and productivity of the metal casting process.**

***Index Terms*— Caster mold, distributed sensing, fiber-optic sensing, metal casting, optical frequency domain reflectometry (OFDR), Rayleigh scattering, thermal mapping.**

I. Introduction

TEMPERATURE measurement in continuous casting molds is an effective tool to monitor process stability and quality of cast metal. The thermal response of a mold provides valuable insights into the solidification behavior of molten metal [1]. In the continuous casting of steel, various quality defects such as longitudinal cracks and stickers (sticker: a layer of metal adhered to a mold surface) originate at the meniscus [2]. These quality defects can lead to cast breakouts if appropriate and timely actions are not taken. It has been demonstrated that longitudinal cracks and stickers cause nonuniform heat flux from the metal to the mold. The nonuniform heat flux induces localized temperature variations at the surface of the mold. Real-time temperature monitoring of the mold can help in the early detection of such quality defects and the prevention of cast breakouts [3]. Moreover, it has been reported that inadequate mold lubrication also causes a substantial deviation in heat flux [2]. The thermal response of a caster mold provides data that can be used to improve mold lubrication and produce high-quality steel products. The meniscus flow velocity of the molten steel in the continuous casting process is another important parameter that has a significant impact on steel quality [4], [5]. Measuring and controlling flow velocity is crucial for ensuring high-quality yield. The thermal profile of a caster mold can be used to estimate flow velocity [6]. Feedback from the temperature measurement system of the mold can be used to adjust flow velocity using a flow control system. In addition to a tool for quality assurance, real-time temperature monitoring of caster molds helps improve production efficiency. Under extreme cases of casting defects, breakouts may occur, which leads to catastrophic damage to equipment, which results in production downtime. Early detection of cast defects and prevention of breakouts can ensure uninterrupted operation. Therefore, real-time temperature monitoring of caster molds provides information that can be useful to improve both quality and productivity.

Conventionally, thermocouples are widely used to perform temperature measurements in caster molds [2], [7]–[10]. However, the inability of thermocouples to perform spatially distributed measurements with high spatial resolution limits their utility in the thermal mapping of caster molds. Furthermore, the instrumentation of caster molds with thermocouples requires machining of the molds to accommodate the probes. Given the sizes of these probes, the machining of the molds introduces problematic unaccounted measurement disturbances. To keep the integrity of the mold intact, the number of thermocouples integrated into the mold plates is limited. The large spacing between temperature measurement points creates dead zones on the mold surface. Localized temperature features appearing in those dead zones cannot be captured. Therefore, many quality defects on the solidified shell go undetected. The measurements from thermocouples are also

Manuscript received August 16, 2021; revised September 27, 2021; accepted October 11, 2021. Date of publication October 19, 2021; date of current version November 3, 2021. This research was supported in part by the Kent D. Peaslee Steel Manufacturing Research Center (PSMRC) at Missouri S&T and the Leonard Wood Institute under Project LWI-2018-006 and in part by the cooperation with the U.S. Army Research Laboratory and was accomplished under Cooperative Agreement W911NF-14-2-0034. The Associate Editor coordinating the review process was Yuya Koyama. *(Corresponding author: Jie Huang.)*

Muhammad Roman, Chen Zhu, Rex E. Gerald II, and Jie Huang are with the Department of Electrical and Computer Engineering, Missouri University of Science and Technology, Rolla, MO 65409 USA (e-mail: jieh@mst.edu).

Damilola Balogun, Laura Bartlett, and Ronald J. O'Malley are with the Department of Material Science and Engineering, Missouri University of Science and Technology, Rolla, MO 65409 USA.

Digital Object Identifier 10.1109/TIM.2021.3121500

affected by electromagnetic systems, such as electromagnetic braking and stirring used for flow control in the continuous casting process. Recently, ultrasonic sensors have been reported for thermal mapping of molds in billet casters [11]. The sensors are mounted on the water jacket, and they can measure mold temperatures in the meniscus region. Although the ultrasonic sensors are non-intrusive, they cannot generate information-rich thermal maps due to a limited number of temperature measurement points. Infrared (IR) cameras are also used for temperature measurements in various steelmaking processes, such as slag detection [12] and steel rolling [13]. However, the accuracy of temperature measurements using an IR camera is affected by the variations in the emissivity of the target surface. Besides, the hot face of a caster mold is not accessible to an IR camera; therefore, thermal mapping of mold surfaces using an IR camera is not easily achievable.

Alternatively, fiber-optic temperature sensors have been explored to achieve high-density thermal mapping of caster molds [6], [14]–[19]. Fiber-optic sensors offer various advantages over conventional sensors, such as the miniaturized size of the optical fiber, immunity to electromagnetic interferences, low thermal capacity, little intrusion into the system, multiplexing capability, remote operation, and the ability to withstand harsh environments. The distinct feature that makes fiber-optic sensors an exciting prospect for thermal mapping of caster molds is the innate capability of fiber-optic sensors to perform distributed sensing. Various fiber-optic sensors were reported for temperature measurements. These sensors include interferometers [20]–[22], fiber Bragg gratings (FBGs) [23], and scattering-based sensors [24], [25]. FBGs attracted considerable interest for thermal mapping of caster molds due to a quasi-distributed sensing capability with a reasonable spatial resolution ($\sim$1 cm), high-temperature resolution ($\sim$0.1 °C), and fast measurement rates (up to a few kHz). Commercial implementations of mold monitoring systems based on FBGs include the HD (high-definition) mold and the OptiMold systems [6], [17]. In the HD mold, 120 FBG sensors, fabricated on 12 optical fibers, were embedded in the copper plate of the mold [15]. Krasilnikov *et al.* [16] reported results using the HD mold. Temperature measurements, recorded during the continuous casting of steel, were used to calculate local heat flux densities. The thickness profile of the solidified shell was subsequently calculated using heat flux measurements. Lieftucht *et al.* [17] reported temperature measurements recorded with the HD mold during the continuous casting of steel. Temperature measurements were used to calculate local heat flux readings over the mold height. Heat flux readings were used to calculate mold levels. The calculated mold levels were compared with steel level readings measured manually. In the OptiMold system, 38 optical fibers, each with 70 FBG sensors, were embedded in the upper half of a copper mold plate [18]. The embedded sensors provided a total of 2660 temperature measurement points. Sedén *et al.* [6] reported results using the OptiMold system in the continuous casting of steel. The thermal profile of the mold was used to estimate the meniscus shape. Additionally, the thermal response of the mold was used to control the flow symmetry of the mold. Spierings *et al.* [19] used thermal data of the mold, collected by the OptiMold system, to investigate mold fluid flow and properties of mold powder.

Although FBGs enjoy commercial success, they have some limitations pointed out hereafter. FBGs can only afford quasi-distributed sensing, so they have measurement dead zones along optical fibers that contain FBGs. Additionally, optical fibers need to be modified to fabricate gratings, which increases the cost of the optical fibers. Moreover, the number of FBGs that can be interrogated along a single continuous optical fiber is limited. Therefore, the thermal mapping of caster molds may require multiple optical fibers. For example, 12 optical fibers were used in the HD mold to achieve 120 FBGs [17], and 38 optical fibers were used in the OptiMold to achieve 2260 FBGs [19]. Multiple lead-in optical fibers require complicated cable management. In addition, multiple optical fibers may require multiple light sources and detectors. For example, three broadband light sources were used to illuminate the optical fibers embedded in the OptiMold.

As opposed to quasi-distributed sensors where index modifications are artificially created inside optical fibers, truly distributed sensors rely on light scattering in unaltered optical fibers. Distributed fiber-optic sensors (DFOS) are mainly based on three types of scattering—Raman, Brillouin, and Rayleigh. The most commonly used techniques to interrogate light scattering in optical fibers are optical time-domain reflectometry (OTDR) [26], optical time-domain analysis (OTDA) [27], and optical frequency-domain reflectometry (OFDR) [28]–[30]. DFOS based on Raman and Brillouin OTDR are suitable for temperature measurements in large structures, such as dams and bridges, due to the extended range of the sensors (kilometers). However, the low spatial resolution of such sensors ($\sim$1 m) makes them less suited for applications in steelmaking, where thermal mappings in compact structures are highly desirable. Considering the fact that sensors based on Raman and Brillouin OTDR and OTDA have low spatial resolution, DFOS based on Rayleigh OFDR were investigated for the thermal mapping of caster molds. The sensing method provides spatially continuous measurements along single-mode optical fibers (SMFs) [31]–[37]. The Rayleigh backscattering (RBS)-based sensing approach provides high spatial resolution ($\sim$0.5 mm), fast measurement rates (a few hundred Hz), and a reasonable sensing length of optical fiber (a few tens of meters). RBS-based temperature sensors were reported for various settings, such as energy generation systems [38], [39] and high-temperature applications in the steel industry [34], [40]. RBS-based sensing could be an exciting prospect for the thermal mapping of caster molds. The ability to provide spatially continuous temperature measurements along an optical fiber can be useful in achieving thermal maps of a caster mold using a single continuous optical fiber, thus making cable management and interrogation a lot easier. Moreover, information-rich thermal maps of caster molds, achieved due to the sub-millimeter spatial resolution of the fiber-optic measurement system, can be instrumental in detecting closely spaced and rapid thermal events occurring at the meniscus.

In this article, RBS-based sensing was used for thermal mapping in a caster mold. An instrumentation method was

devised to embed an optical fiber in a copper mold plate for spatially distributed temperature measurements. A high numerical aperture (NA) optical fiber, with high macrobending loss resistance, was used to instrument a compact mold plate using a single continuous looped optical fiber. The instrumented mold plate was immersed in cast-iron melt (C 3.10%, Si 1.87%, Mn 0.5%, Cr 0.16%) at 1450 °C and in steel melt (C 0.2%, Si 2.0%, Mn 0.07%, Al 0.08%) at 1600 °C. The silica optical fibers used in the mold instrumentation cannot withstand such high temperatures. Therefore, the optical fibers were protected from direct exposure to the molten metal. The work reported here was intended to measure temperatures in the mold as a result of transient heat transfer from metal to the mold during immersion and solidification. The maximum temperatures recorded by the embedded fiber-optic sensors were 469 °C and 388 °C in the cast-iron and steel dip tests, respectively. In both the cases, the metered temperatures remained well below the maximum temperature measurement capability of RBS-based fiber-optic sensors, which is approximately 700 °C–750 °C for unmodified silica optical fibers [41]. Thermal maps of the mold, generated during the immersion of the mold into the molten metal and solidification of the shell against the mold wall, provided valuable insights into the solidification behavior.

II. RBS-Based Temperature Measurements and OFDR Interrogation

RBS-based sensing is a distributed sensing method that provides spatially continuous temperature measurements along SMFs. The RBS effect derives from the scattering of light from fluctuations in refractive index in an optical fiber. The RBS-based temperature measurements rely on the fact that temperature variations cause shifts in the RBS spectra. The shifts in the RBS spectra are attributed to the changes in the refractive index and the length of an optical fiber as a result of the changes in temperature. The RBS shift ($\Delta\lambda$) caused by a change in temperature (ΔT) is given as:

$$\Delta\lambda = \lambda(\alpha + \zeta)\Delta T \tag{1}$$

where λ is the operating wavelength, α is the thermal expansion coefficient ($0.55 \times 10^{-6}/°C$), and ζ is the thermo-optic coefficient ($8.5 \times 10^{-6}/°C$) of the optical fiber.

A commercially available OFDR interrogator (LUNA ODiSI 6108) was used to interrogate RBS signals obtained from the optical fiber under test. The interrogator used a tunable laser source with a 50 nm tuning range (1515–1565 nm) and a 1000 nm/s tuning speed. The highest spatial resolution achieved using the interrogator was 0.65 mm (for a fiber length of up to 2.5 m with a measurement acquisition rate of 62 Hz). The maximum measurement acquisition rate provided by the interrogator was 250 Hz (for a fiber length of up to 2.5 m with a spatial resolution of 2.6 mm). The measurement acquisition rate varies depending on the length of the sensing fiber and the spatial resolution used in the measurements. For a given spatial resolution, the measurement acquisition rate decreases with an increase in sensing fiber length. Similarly, for a given length of the sensing fiber, the measurement acquisition rate decreases with an increase in spatial resolution. The interrogator automatically adjusts the measurement acquisition rate based on the length of the sensing fiber used in the experiment and the value of spatial resolution selected for the measurements. The interrogator can perform distributed temperature measurements along a single-mode fiber over distances of up to 50 m.

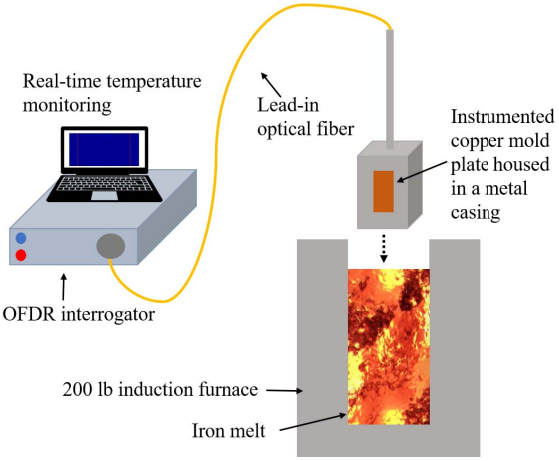

Fig. 1. Schematic of the experiment setup of the dip test using a copper mold instrumented with distributed fiber-optic temperature sensors.

III. Experimental Setup for the Dip Test

The thermal mapping of a caster mold has great value in metal casting. As discussed earlier, real-time temperature monitoring of a mold has a significant role in improving the quality and productivity of the cast. The potential of RBS-based fiber-optic temperature measurement for real-time thermal mapping of the caster mold was demonstrated in a dip test. An instrumentation method was devised to embed optical fibers in copper mold plates. The objective was to conduct a dip test with an instrumented mold and generate thermal maps of the mold plate during immersion and solidification. Fig. 1 shows a schematic of the experimental setup used to conduct the dip test with a mold instrumented with optical fibers. The dip test was conducted in a 200 lb induction furnace in the Missouri S&T foundry laboratory. A copper mold plate (100 mm × 50 mm × 12 mm thick) was instrumented with an optical fiber for temperature measurements. The mold plate was housed in a metal casing to protect fiber loops from the molten metal during the dip test. One end of the optical fiber, used in the instrumentation of the mold plate, was connected to the OFDR interrogator. The other end of the optical fiber was placed inside the metal casing. The following sections present more details about the mold instrumentation and the experimental setup of the dip test.

A. High NA Fiber as a Sensing Device

The RBS-based temperature measurement system exploits an unmodified SMF as a sensing device. The optical fiber commonly used for the RBS-based measurements is a communication grade standard SMF. To instrument a mold plate using a single continuous optical fiber, the optical fiber

needs to be looped, making multiple sensing paths. However, the compact mold plate requires sharp bending of the optical fiber for the embedding process. The standard SMF exhibits significant attenuation in the RBS signal due to sharp bends. The attenuation in the RBS signal deteriorates the signal-to-noise ratio (SNR) and leads to the failure of OFDR measurements [42]. An optical fiber with a high NA was used to address the issue of signal attenuation due to bending. An optical fiber with a high NA diminishes macrobending loss and allows multiple sharp bends of the fiber under test [43]. The single-mode high NA optical fiber used to instrument the mold was UHNA1 from Nufern (East Grandby, CT). The UHNA1 fiber has a core diameter of 2.5 μm, NA of 0.28, mode field diameter of 4.8 $\pm$ 0.3 μm at the wavelength of 1550 nm, and a cladding diameter of 125 $\pm$ 1 μm. The high NA fiber can be wrapped to a radius of a few millimeters without experiencing significant attenuation in the RBS signal.

B. Temperature Coefficients for the High NA Fiber

The frequency shift response of the fiber-optic measurement system, as a result of the changes in temperature, was measured and calibrated before the mold instrument was fit with the fiber. To conduct a temperature-ramp experiment, a section of a high NA optical fiber was placed in a tube furnace (Thermo scientific TF55030A-1). One end of the fiber was connected to the OFDR interrogator, and the other end was spliced to a coreless fiber positioned outside the furnace. The coreless fiber was used to reduce reflections from the end face of the high NA optical fiber. A K-type thermocouple, connected to a data logger (Graphtec GL220), was placed together with the optical fiber for temperature measurements at a single position in the furnace. To compare a frequency shift profile recorded using the OFDR interrogator to the temperature profile measured with the thermocouple system, a position on the optical fiber, close to the tip of the thermocouple probe, was identified using a point heating source before the experiment. The temperature inside the furnace was increased from room temperature (22 °C) to 740 °C at an average ramp-up rate of 20 °C/min. The power to the furnace was then turned off, and the furnace was allowed to cool down. When the temperature dropped to 400 °C, the power was turned on again. The temperature was increased from 400 °C to 740 °C. During the entire duration of the temperature-ramp experiment, the OFDR interrogator measured shifts in the Rayleigh spectra along the length of the optical fiber with an update rate of 1 Hz. The thermocouple system measured temperature at a single position with an update rate of 1 Hz. Fig. 2 shows measurements from both the fiber-optic and the thermocouple systems during the temperature-ramp experiment. The frequency shift and temperature measurements recorded during the first ramp-up (22 °C to 740 °C) were used for the calibration. The frequency shift data were converted into temperature using a second-order polynomial fitting, as shown in Fig. 2(a). The coefficients of the second-order polynomial ($p1$, $p2$, and $p3$) that relate frequency shift (F) to temperature (T) are provided in Fig. 2(a). The same calibration coefficients were used to convert frequency shift measurements into temperature measurements for the two successive temperature ramp-down and ramp-up processes. The measurements recorded using the OFDR interrogator and thermocouple systems exhibited good agreement for the entire duration of the temperature-ramp experiment, as evident from Fig. 2(b). The experiment not only provided calibration coefficients but also demonstrated the reliability of OFDR measurements, using a high NA fiber as a sensing device, for temperatures up to 740 °C.

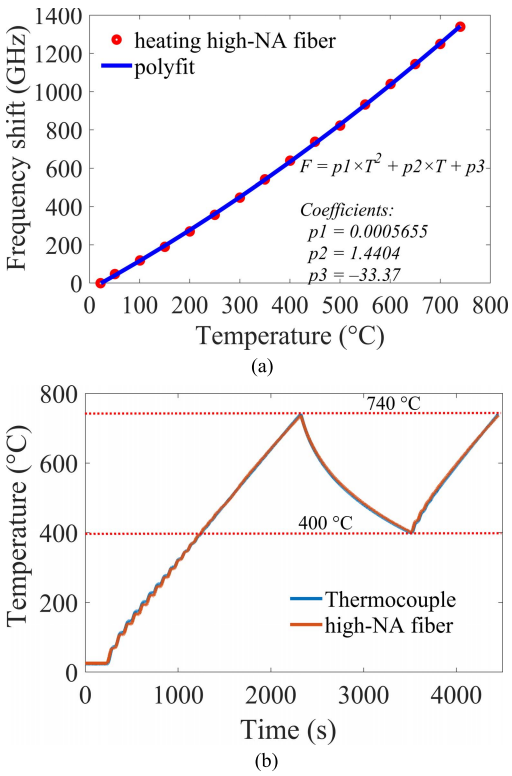

Fig. 2. Responses of the fiber-optic and thermocouple systems during temperature ramp-up and ramp-down processes. (a) Plot of the frequency shift response, recorded by the fiber-optic system, for various temperatures metered by the thermocouple placed in the furnace. Frequency shift data were converted into temperature data using a second-order polynomial fitting. F: frequency shift; T: temperature; $p1$, $p2$, and $p3$: coefficients of the second-order polynomial. (b) Fiber-optic and thermocouple temperature measurements during temperature ramp-up and -down processes.

C. Instrumenting a Copper Mold Plate With Optical Fibers

A copper plate (100 mm × 50 mm × 12 mm thick) was used to machine a mold that was instrumented with optical fibers. The dimensions of the plate were selected so that the dip test could be conducted in a 200 lb induction furnace in a foundry laboratory. The objective of the test was to generate 2-D thermal maps of the mold plate in real-time using an embedded fiber-optic sensor during immersion of the mold into the molten metal and subsequent solidification of the metal shell against the mold surface. An optical fiber should maintain good thermal contact with the hot face to measure temperature variations at the surface of the mold. An optical fiber bonded to the surface of the mold can experience thermally induced strains due to the mismatch of the coefficient of thermal expansions (CTEs) of the optical fiber (fused silica CTE:

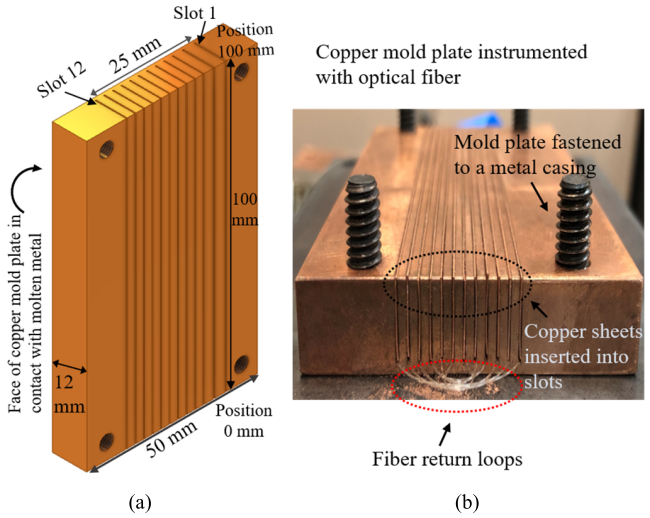

Fig. 3. Schematic of the EDM-machined copper mold plate and photograph of the same after instrumentation with an optical fiber. (a) Schematic of the copper mold plate (100 mm × 50 mm × 12 mm) used in the dip test. Twelve slots, each 350 μm wide, were machined from the back face of the mold plate to within 1 mm of the front face. (b) Photograph of the instrumented mold plate. The slots on the copper mold plate were instrumented with a single continuous optical fiber configured with multiple return loops at both ends of the mold plate. The slots were backfilled with copper powder and copper sheets. The mold plate was fastened to a metal casing.

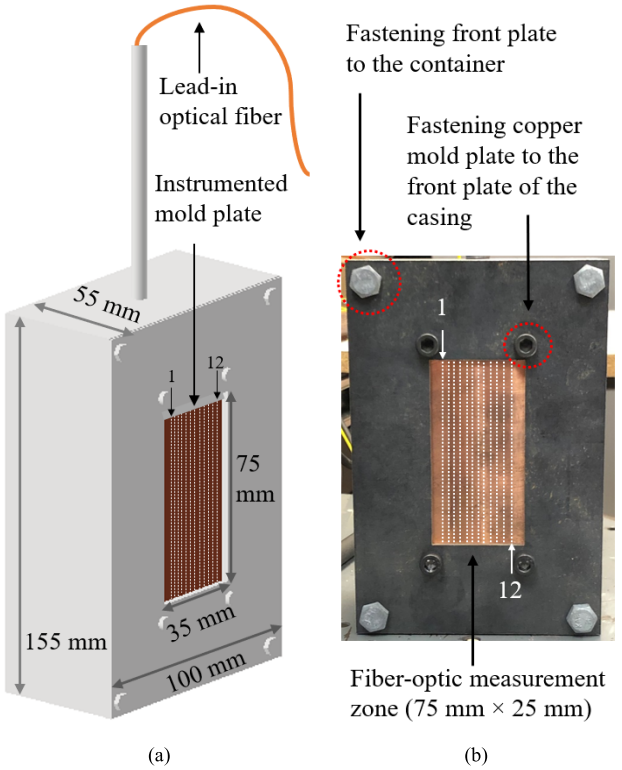

Fig. 4. Schematic and photograph of the instrumented copper mold plate housed in a metal casing (a.k.a. the test paddle). (a) Schematic of the mold plate housed in a metal casing. The instrumented mold plate was attached to the front metal plate of the casing. The front plate was then fixed to the casing. The casing protected the back face of the mold plate and fiber loops from direct exposure to the molten metal during the dip test. Twelve white dotted lines represent the 12 embedded fiber sections. (b) Photograph of the front face of the metal casing mounted to the instrumented copper mold plate.

0.55 × 10^{-6}/°C) and the material of the mold plate (copper CTE: 17 × 10^{-6}/°C). Therefore, the optical fiber should be thermally connected to, but mechanically decoupled from, the hot face of the mold. Moreover, an embedded fiber should minimally interfere with the heat flow inside the mold. An embedding scheme was devised to achieve the aforementioned objectives. Fig. 3 shows a schematic of an electrical discharge machining (EDM)-machined copper mold plate and a photograph of the plate after instrumentation with an optical fiber. Twelve deep slots (each 350 μm wide) were machined longitudinally from the back face of the mold plate to within 1 mm of the hot face using wire EDM as shown in Fig. 3(a). The separation between two neighboring slots was 2 mm. Fig. 3(b) shows a photograph of the mold instrumented with an optical fiber. A high NA SMF was used to instrument all 12 slots. The high macrobending loss resistance of the high NA fiber enabled the instrumentation of all 12 slots using a single continuous optical fiber with multiple return loops. For each slot, a section of the optical fiber was loosely placed at the base of the slot. The slot was backfilled with copper powder (325 mesh) up to a height of 2 mm from the base of the slot. The remaining space in the slot was filled by inserting a thin copper sheet (100 mm × 9 mm × 0.32 mm thick) into the slot. The use of thin machined slots from the back face of the mold plate minimized interference with the hot face heat flow in the mold, providing a more uniform surface exposed to the molten metal. The deep slots ensured that the optical fiber close to the hot face allows the capture of rapid thermal events. The loose fiber surrounded by copper powder provided improved heat flow uniformity while ensuring that no thermally induced strain was transferred to the optical fiber from the copper mold plate as the mold plate was heated. The thin copper sheets, inserted into the slots, improved the heat flow inside the mold.

D. Casing for the Mold

A mild steel (AISI 1018 grade) casing was designed to protect the optical fiber loops and the copper mold plate's cold end from direct contact with the molten metal. Fig. 4 includes a schematic and a photograph of the EDM machined copper mold plate housed in the metal casing. The casing consists of two parts, a 3 mm thick, 155 mm × 100 mm front plate to which the instrumented copper mold plate was fastened and a 52 mm thick, 155 × 100 mm container that housed the return loops and the lead-out optical fiber. The fiber was then passed through a 3/4 -npt pipe and connected to the interrogator. With the inner wall of the test casing was lined with an alumino-silicate ceramic fiber paper, heat transfer was predominantly confined to one direction only, from the metal to the hot face of the mold. The steel casing was coated with an alcohol-based zircon wash to facilitate easy recovery of the solidified shell.

E. Test Assembly and the RBS Signal From the Fiber Under Test

To keep the OFDR interrogator at a safe distance from the high-temperature environment of the induction furnace,

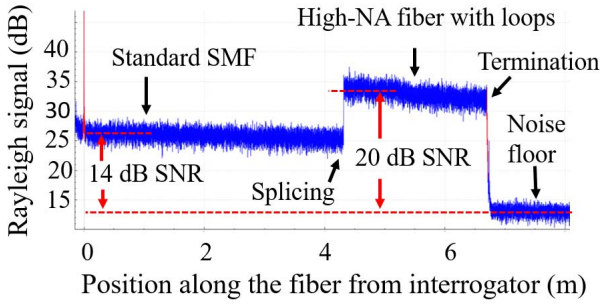

Fig. 5. Relative intensity of the Rayleigh backscattering signal along the lead-in SMF and the embedded high NA fiber. The low macrobending loss of the high NA fiber ensured good signal strength despite having multiple permanent sharp bends in the fiber resulting from the embedding process.

a 4.3 m long lead-in standard SMF was used. The standard SMF was spliced to a 2.4 m long high NA fiber using a fusion splicer (Fujikura 70S). The other end of the high NA fiber was spliced to a 30 cm long coreless fiber to reduce reflections from the high NA fiber's end face. The copper mold plate was instrumented with the high NA fiber, as discussed earlier in Section III-C. Fig. 5 shows the RBS signal obtained from the lead-in standard SMF and the high NA fiber. The RBS signal was recorded after the mold was instrumented with the fiber. A higher dopant concentration in the core and improved capture fraction due to the high NA of the fiber may account for the ∼6 dB enhancement in the RBS signal obtained from the fiber [44]. To instrument 12 slots using a single continuous high NA fiber, 11 return loops of the fiber were configured. The bending radii of the fiber loops ranged from as large as 30 mm down to as small as 5 mm. It is evident from Fig. 5 that the SNR for the looped high-NA fiber is better than the SNR of the straight lead-in standard SMF.

IV. Dip Test

The dip test procedure involved induction melting of a gray cast-iron charge (C 3.10%, Si 1.87%, Mn 0.5%, Cr 0.16%) in a 200 lb coreless induction furnace. The temperature of the melt was measured using a handheld temperature probe with a platinum-based thermocouple (Heraeus Digilance V). When the temperature of the melt was 1450 °C, the test paddle was slowly lowered into the melt crucible and held for 4 s before withdrawal. An iron shell was formed on the mold wall. Temperature measurements were performed continuously throughout the immersion and solidification process. The spatially distributed temperatures along the length of the optical fiber were metered with a 0.65-mm spatial resolution. The measurements were recorded with an update rate of 25 Hz. The width of the mold plate, where temperature points were measured, was 25 mm. There were 1380 distinct temperature measurement points over an area of 75 mm × 25 mm. To the best of our knowledge, such a high-density thermal mapping scheme for a metal casting mold has not been reported previously. The high density of measurements provides a very detailed thermal response of the mold as the mold transfers heat from the molten metal during solidification.

V. Results and Discussion

Fig. 6 shows a schematic of the test paddle used in the dip test and spatially distributed temperature profiles along embedded fiber sections. The machining and instrumentation of the mold plate, as shown in Fig. 6(a), was discussed in Section III-C. Fig. 6(b) shows a thermal map of the mold surface during the dip test (when the mold was fully immersed). The spatially distributed temperature measurements were used to generate thermal maps of the mold surface at 1 mm from the hot face where the fiber sections were embedded. Temperature values were sampled with 0.65 mm resolution along the y-axis (corresponding to the spatial resolution of the OFDR interrogator) and with 2 mm resolution along the x-axis (corresponding to the spacing between adjacent optical fiber sections). The thermal maps were generated by MATLAB R2018b using pseudocolor plots with bilinear interpolation, and the colors represent a range of temperatures. The jet color scheme with 1024 color levels was used to obtain smoother transitions between colors. Fig. 6(c) shows spatially distributed temperature profiles along 12 fiber sections embedded in the mold plate. The temperature profiles are shown at four times during the dip test, labeled $t1$–$t4$. $t1 = 0$ s: before immersing the mold into the molten metal; $t2 = 1$ s: when the mold was partially immersed into the molten metal; $t3 = 3.5$ s: when the mold was fully immersed; and $t4 = 8$ s: after the mold was taken out of the crucible with a metal shell solidified on the mold wall. Before immersion, at time $t1$, all 12 embedded fiber sections uniformly registered room temperature (∼25 °C). A temperature rise was observed during immersion, and a temperature gradient was also observed along the length of the mold. The lower part of the mold registered a higher temperature, while the upper part registered a lower temperature because the mold was partially immersed at that time. The temperature profiles along the embedded fiber sections exhibited a similar trend in the temperature gradients when the mold was fully immersed. The lower part was hotter than the upper part of the mold. Temperature gradients began to dissipate shortly after the mold was removed from the molten metal due to the redistribution of heat on the mold surface, as depicted by temperature profiles at time $t4 = 8$ s. The high spatial resolution (0.65 mm) and fast measurement rate (25 Hz) of the fiber-optic temperature measurement system made it possible to monitor a detailed thermal response of the mold during the immersion and solidification process. The information-rich thermal history of the mold provided useful insights into the casting process.

Fig. 7 shows the thermal maps of the mold surface at different time instances during the dip test. The thermal maps indicate that the temperature began increasing at the bottom of the mold plate, which agrees with the test procedure because the immersion into the molten metal started at the bottom of the test paddle mold plate. When the mold was fully immersed, the entire area of the mold showed a temperature rise. However, a significant temperature difference was observed between the lower and upper parts of the mold. The heating rate of the mold was attributed to solidification kinetics and, subsequently, the solidified shell profile.

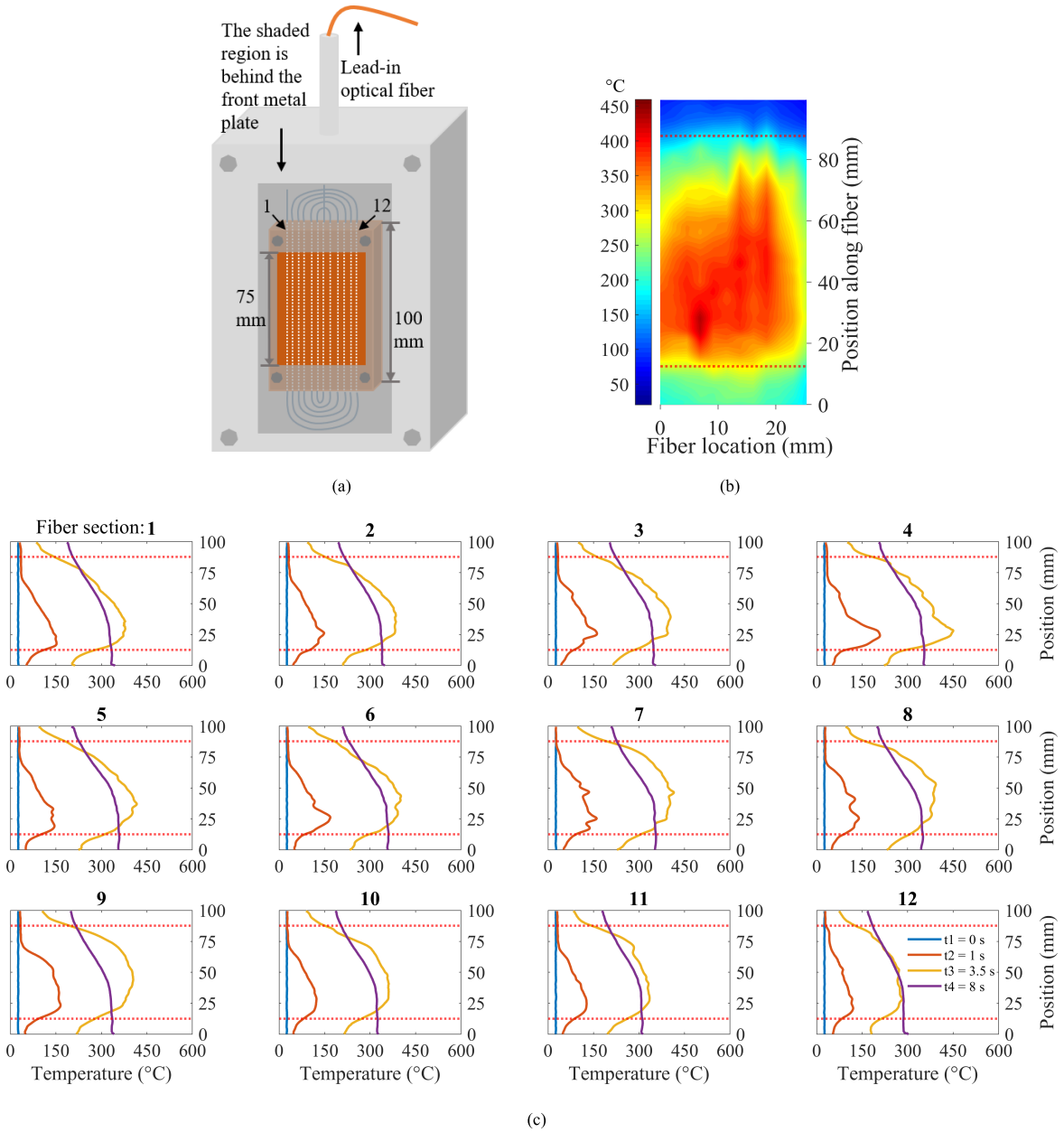

Fig. 6. Schematic of the test paddle and spatially distributed temperature profiles along the embedded optical fiber sections. (a) Schematic of the instrumented mold plate housed in a metal casing. The optical fiber sections embedded in the mold plate and optical fiber return loops at the top and bottom of the mold are shown. b) Thermal map of the mold plate during the dip test. The length between the two red dotted lines corresponds to the 75 mm long surface of the 100 mm long mold plate, which was exposed to the molten metal (c) Spatially distributed temperature profiles along 12 adjacent embedded optical fiber sections at four instances of time during the immersion and solidification process. $t1 = 0$ s: a time before immersing the mold into the molten metal, $t2 = 1$ s: during immersion when the mold was partially immersed into the molten metal, $t3 = 3.5$ s: when the mold was fully immersed, and $t4 = 8$ s: after the mold was taken out of the crucible with a shell solidified against the face of the mold. The graph labeled "Fiber section: **1**" shows temperature profiles along the leftmost embedded optical fiber section (viewed from the top surface of the mold plate, which was exposed to the molten metal), and the graph labeled **12** corresponds to the right-most embedded optical fiber section.

The solidified shell morphology correlated well with the thermal profile, as regions with higher temperatures in the thermal profile corresponded to areas on the shell that were thicker. The temperature profile suggests that solidification of the metal shell was nonuniform, which agreed with direct observations of the shell thickness. The use of thermal maps in this manner will help identify areas where thinning of the shell may likely occur.

The generally higher temperature at the lower part of the mold was the result of the slightly longer residence time in the molten iron due to the finite speed of immersion into and withdrawal from the bath. The lower temperature at the top of the mold was due to its slightly shorter residence time in the molten iron bath. The low-temperature zone on the mold surface indicated a reduced heat flux from the shell to the mold. Another possible cause for the reduced heat flux in the upper part of the mold is the formation of an air gap between the shell and the mold surface during shell growth, caused by shell distortion. The reduced heat flux resulted in reduced shell thickness, which could eventually lead to cast breakout.

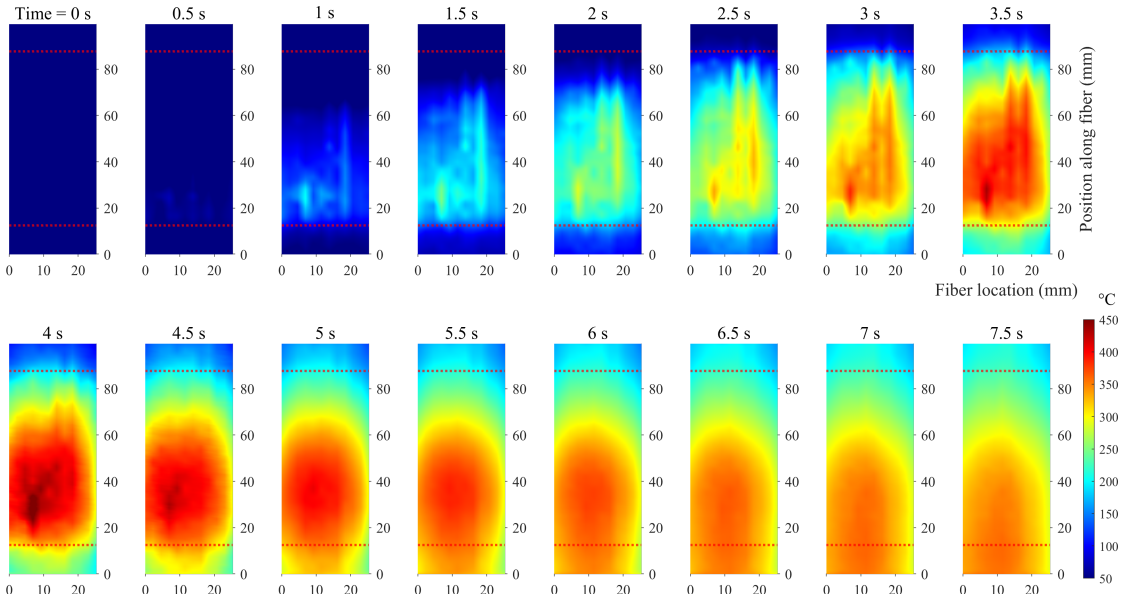

Fig. 7. Thermal maps of the copper mold plate during the immersion and solidification process of a dip test. The immersion started at $t = 0.5$ s. At $t = 2$ s, the mold was fully immersed in the molten metal. The mold plate remained immersed for 4 sec until $t = 6$ s. At $t = 7.5$ s, the mold was out of the crucible with a shell solidified against the face of the mold.

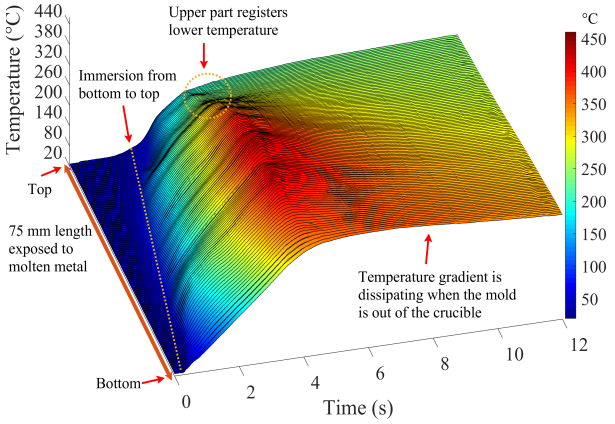

Fig. 8. Spatially distributed temperature profile along one of the embedded fiber sections (the fiber section embedded in slot 6, numbered from the left of the mold) during the immersion and solidification process.

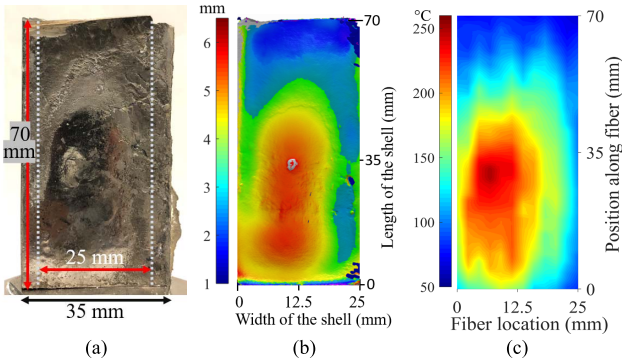

Fig. 9. Side-by-side comparison of a photograph of the solidified steel shell, the thickness map of the shell, and a thermal map of the mold plate. (a) Photograph of the mold face side of the shell (70 mm × 35 mm). The photograph was flipped horizontally to make the orientation of the shell the same as the orientations of the thickness map of the shell and the thermal map of the mold. The width between the two white dotted lines is the 25 mm wide surface of the 35 mm wide shell, which corresponds to the 25 mm wide surface of the mold plate where fiber sections were embedded for temperature measurements. (b) Thickness map (mm) of the solidified steel shell. (c) Thermal map of the mold plate during solidification.

Fig. 8 shows a spatial–temporal thermal map for one of the embedded fiber sections, the fiber section embedded in slot 6, numbered from the left of the mold. Slot 6 was close to the midplane of the mold. The spatially distributed temperature profile along the 75 mm length of the fiber (the length of the mold exposed to molten metal) is shown during the immersion of the mold and during solidification and cooling of the shell. The temperature rise from the bottom to the top of the mold during immersion is clearly visible. Moreover, the spatial–temporal profile illustrates that the temperature in the upper part remained lower than the temperature in the lower part of the mold. Similarly, the spatial–temporal thermal profiles for the remaining 11 sections of the fiber can be obtained to investigate the thermal behavior of other zones of the mold.

Another dip test was conducted in a steel bath using the same experimental setup. The thermal profiles of the mold plate were measured continuously throughout the immersion and solidification process. A steel shell (C 0.2%, Si 2.0%, Mn 0.07%, Al 0.08%) was formed on the mold wall. A complete 3-D scan of the solidified shell was performed using a 40 μm point resolution blue light scanner (OptimScan-5M) to measure the thickness profile of the shell. The scanned data were processed in MATLAB R2019a to generate a thickness map of the shell. Fig. 9 shows a photograph of the solidified shell, the thickness map of the shell, and a thermal map of the mold during the solidification process. Fig. 9(a) shows a photograph of the mold face side of the shell (70 mm × 35 mm). The width between the two white dotted lines is the 25 mm wide surface of the 35 mm wide shell, which corresponds to the 25 mm wide surface of the mold plate where fiber sections were embedded for temperature measurements. A good correlation was observed between the

thickness map of the solidified shell [Fig. 9(b)] and the thermal map of the mold [Fig. 9(c)]. The regions reporting higher temperatures in the thermal profile corresponded to areas on the shell that were thicker. The lower temperature regions on the mold surface corresponded to the thinner areas of the shell. The correlation between the thickness map of the solidified shell and the thermal map of the mold demonstrates that RBS-based fiber-optic temperature measurements are very useful for real-time thermal mapping of the caster mold.

VI. Conclusion

We reported and demonstrated a method to embed RBS-based fiber-optic temperature sensors into a copper mold plate to generate thermal maps of the mold during the metal casting process. Deep slots were machined into the mold, using a wire EDM, from the back face of the mold to within 1 mm of the front face (hot face) to accommodate sensor installation into the mold plate. All slots were instrumented using a single continuous optical fiber with multiple return loops at both ends of the mold plate. A single optical fiber was used, providing for simple cable management and interrogation of the fiber sensor under test conditions. The instrumented mold plate was used to conduct a cast-iron dip test and a steel dip test in a 200 lb induction furnace. 2-D thermal maps of the mold plate were generated during immersion of the mold into crucible and solidification of a metal shell against the mold wall. The localized and rapid temperature features observed for the mold wall were successfully mapped using a fiber-optic sensor that was embedded close to the mold surface (at a depth of 1 mm). RBS-based measurements were performed with a high spatial resolution (0.65 mm) and a fast measurement rate (25 Hz). The information obtained from the thermal maps provided valuable insights into the solidification behavior. The thickness map of the solidified steel shell was compared with a thermal map of the mold plate, and good correlations of features were observed between the two measurements. The dip test experiments demonstrated that RBS-based fiber-optic sensing is an effective method for real-time temperature monitoring of caster molds. Investigating the information-rich thermal response of the mold can be useful for improving the quality of the metal and the productivity of the casting process.

References

[1] B. G. Thomas, M. S. Jenkins, and R. B. Mahapatra, "Investigation of strand surface defects using mould instrumentation and modelling," *Ironmaking Steelmaking*, vol. 31, no. 6, pp. 485–494, Dec. 2004.

[2] S. Carless, A. Kamperman, A. Westendorp, and J. Brockhoff, "Optimization of surface quality through mold thermal monitoring," *Iron Steel Technol.*, vol. 8, no. 7, pp. 84–92, 2011.

[3] W. H. Emling and S. Dawson, "Mold instrumentation for breakout detection and control," in *Proc. Steelmaking Conf.*, 1991, pp. 161–181.

[4] S. M. Cho *et al.*, "Measurement of transient meniscus flow in steel continuous casters and effect of electromagnetic braking," in *Sensors, Sampling, and Simulation for Process Control*. Hoboken, NJ, USA: Wiley, 2011, pp. 59–66.

[5] Q. He, Z. Su, Z. Xie, Z. Zhong, and Q. Yao, "A novel principle for molten steel level measurement in tundish by using temperature gradient," *IEEE Trans. Instrum. Meas.*, vol. 66, no. 7, pp. 1809–1819, Jul. 2017.

[6] M. Sedén *et al.*, "Development of enhanced mold flow control in slab casting," SCANMET V, Luleå, Sweden, Tech. Rep., Jun. 2016, Paper 111.

[7] G. Xia *et al.*, "Investigation of mould thermal behaviour by means of mould instrumentation," *Ironmaking Steelmaking*, vol. 31, no. 5, pp. 364–370, Oct. 2004.

[8] M. Suzuki *et al.*, "Analysis of heat transfer and solidifying shell deformation in mold in high speed continuous casting of peritectic medium carbon steels," in *Proc. Steelmaking Conf.*, 1998, pp. 165–171.

[9] T. T. Natarajan, S. R. Story, T. J. Piccone, and K. D. Van Ness, "Peritectic range study using mold thermocouple data," in *Proc. AISTech*, no. 412, 2017, pp. 1645–1654.

[10] B. G. Thomas, M. A. Wells, and D. Li, "Monitoring of meniscus thermal phenomena with thermocouples in continuous casting of steel," in *Sensors, Sampling, and Simulation for Process Control*. Hoboken, NJ, USA: Wiley, 2011, pp. 119–126.

[11] I. Mazza, S. Miani, G. Schiavon, and S. Spagnul, "Real-time and contactless mold thermal monitoring: Improving metallurgy, quality and productivity of billets and Blooms," *BHM Berg Hüttenmännische Monatshefte*, vol. 165, no. 1, pp. 11–18, Jan. 2020.

[12] R. Strąkowski, K. Pacholski, B. Więcek, R. Olbrycht, W. Wittchen, and M. Borecki, "Estimation of FeO content in the steel slag using infrared imaging and artificial neural network," *Measurement*, vol. 117, pp. 380–389, Mar. 2018.

[13] R. Usamentiaga, D. F. Garcia, and J. M. Perez, "High-speed temperature monitoring for steel strips using infrared line scanners," *IEEE Trans. Ind. Appl.*, vol. 56, no. 3, pp. 3261–3271, May 2020.

[14] B. G. Thomas and M. K. Okelman, "Implementation of temperature and strain micro-sensors into a casting mold surface," in *Sensors, Sampling, and Simulation for Process Control*. Hoboken, NJ, USA: Wiley, 2011, pp. 127–134.

[15] J. Wans, D. Lieftucht, C. Geerkens, M. Arzberger, and M. Reifferscheid, "HD mold - Caster assistance system to increase product quality," in *Proc. AISTech Iron Steel Technol. Conf.*, vol. 2, May 2013, pp. 1385–1391.

[16] A. Krasilnikov *et al.*, "Online shell thickness calculation operating in a new fibre-optical based mould monitoring system," in *Proc. 5th Int. Congr. Sci. Technol. Steelmaking (ICS)*, Dresden, Germany, Oct. 2012, pp. 1–9.

[17] D. Lieftucht, M. Reifferscheid, T. Schramm, A. Krasilnikov, and D. Kirsch, "HD mold—A new fiber-optical-based mold monitoring system," *Iron Steel Technol.*, vol. 10, pp. 87–95, May 2013.

[18] G. Hedin *et al.*, "Exploring opportunities in mold temperature monitoring utilizing fiber Bragg gratings," in *Proc. 5th Int. Conf. Process Develop. Iron Steelmaking*, Jun. 2016, Paper 36.

[19] T. Spierings, A. Kamperman, H. Hengeveld, J. Kromhout, and E. Dekker, "Development and application of fiber Bragg gratings for slab casting," in *Proc. AISTech*, May 2017, pp. 1655–1664.

[20] C. Zhu, Y. Zhuang, B. Zhang, R. Muhammad, P. P. Wang, and J. Huang, "A miniaturized optical fiber tip high-temperature sensor based on concave-shaped Fabry–Perot cavity," *IEEE Photon. Technol. Lett.*, vol. 31, no. 1, pp. 35–38, Nov. 1, 2019.

[21] X.-G. Li *et al.*, "Measurement of magnetic field and temperature based on fiber-optic composite interferometer," *IEEE Trans. Instrum. Meas.*, vol. 66, no. 7, pp. 1906–1911, Jul. 2017.

[22] C. Han, H. Ding, Q. Zhang, and C. Zhao, "Miniature Fizeau interferometric thermometer," *IEEE Trans. Instrum. Meas.*, vol. 69, no. 11, pp. 9237–9242, Nov. 2020.

[23] R. Gassino, G. Perrone, and A. Vallan, "Temperature monitoring with fiber Bragg grating sensors in nonuniform conditions," *IEEE Trans. Instrum. Meas.*, vol. 69, no. 4, pp. 1336–1343, Apr. 2020.

[24] A. Ukil, H. Braendle, and P. Krippner, "Distributed temperature sensing: Review of technology and applications," *IEEE Sensors J.*, vol. 12, no. 5, pp. 885–892, May 2012.

[25] C. Zhu, R. E. Gerald, and J. Huang, "Progress toward sapphire optical fiber sensors for high-temperature applications," *IEEE Trans. Instrum. Meas.*, vol. 69, no. 11, pp. 8639–8655, Nov. 2020.

[26] M. K. Barnoski and S. M. Jensen, "Fiber waveguides: A novel technique for investigating attenuation characteristics," *Appl. Opt.*, vol. 15, no. 9, p. 2112, 1976.

[27] Y. Dong, H. Zhang, L. Chen, and X. Bao, "2 cm spatial-resolution and 2 km range Brillouin optical fiber sensor using a transient differential pulse pair," *Appl. Opt.*, vol. 51, no. 9, pp. 1229–1235, Mar. 2012.

[28] Z. Yao, T. Mauldin, Z. Xu, G. Hefferman, and T. Wei, "An integrated OFDR system using combined swept-laser linearization and phase error compensation," *IEEE Trans. Instrum. Meas.*, vol. 70, pp. 1–8, 2021.

[29] G.-M. Ma *et al.*, "High-resolution temperature distribution measurement of GIL spacer based on OFDR and ultraweak FBGs," *IEEE Trans. Instrum. Meas.*, vol. 69, no. 6, pp. 3866–3873, Jun. 2020.

[30] B. J. Soller, D. K. Gifford, M. S. Wolfe, and M. E. Froggatt, "High resolution optical frequency domain reflectometry for characterization of components and assemblies," *Opt. Exp.*, vol. 13, no. 2, p. 666, 2005.
[31] Y. Du, S. Jothibasu, Y. Zhuang, C. Zhu, and J. Huang, "Unclonable optical fiber identification based on Rayleigh backscattering signatures," *J. Lightw. Technol.*, vol. 35, no. 21, pp. 4634–4640, Nov. 1, 2017.
[32] C. Zhu, Y. Zhuang, and Y. Chen, "Distributed fiber-optic pressure sensor based on bourdon tubes metered by optical frequency-domain reflectometry," *Opt. Eng.*, vol. 58, no. 7, p. 1, Apr. 2019.
[33] S. Jothibasu *et al.*, "Spatially continuous strain monitoring using distributed fiber optic sensors embedded in carbon fiber composites," *Opt. Eng.*, vol. 58, no. 7, p. 1, Feb. 2019.
[34] M. Roman *et al.*, "A spatially distributed fiber-optic temperature sensor for applications in the steel industry," *Sensors*, vol. 20, no. 14, p. 3900, 2020.
[35] Y. Du, Q. Yang, and J. Huang, "Soft prosthetic forefinger tactile sensing via a string of intact single mode optical fiber," *IEEE Sensors J.*, vol. 17, no. 22, pp. 7455–7459, Nov. 2017.
[36] Y. Du, S. Jothibasu, Y. Zhuang, C. Zhu, and J. Huang, "Rayleigh backscattering based macrobending single mode fiber for distributed refractive index sensing," *Sens. Actuators B, Chem.*, vol. 248, pp. 346–350, Sep. 2017.
[37] Y. Du, Y. Chen, Y. Zhuang, C. Zhu, R. Gerald, and J. Huang, "A uniform strain transfer scheme for accurate distributed optical fiber strain measurements in civil structures," *Inventions*, vol. 3, no. 2, p. 30, May 2018.
[38] S. Rizzolo *et al.*, "Vulnerability of OFDR-based distributed sensors to high γ-ray doses," *Opt. Exp.*, vol. 23, no. 15, p. 18997, 2015.
[39] S. Rizzolo *et al.*, "Real time monitoring of water level and temperature in storage fuel pools through optical fibre sensors," *Sci. Rep.*, vol. 7, no. 1, pp. 1–10, Dec. 2017.
[40] M. Roman, D. Balogun, R. E. Gerald, II, L. Bartlett, J. Huang, and R. J. O'Malley, "Peritectic behavior detection in the Fe-C-Mn-Al-Si steel system using fiber optic temperature mapping," in *Proc. Iron Steel Technol. Conf. (AISTech)*, 2020, pp. 822–833.
[41] K. M. McCary, B. A. Wilson, A. Birri, and T. E. Blue, "Response of distributed fiber optic temperature sensors to high-temperature step transients," *IEEE Sensors J.*, vol. 18, no. 21, pp. 8755–8761, Nov. 2018.
[42] K. Naeem, Y. Kwon, Y. Chung, and I. Kwon, "Bend-loss-free distributed sensor based on Rayleigh backscattering in Ge-doped-core PCF," *IEEE Sensors J.*, vol. 18, no. 5, pp. 1903–1910, Mar. 2018.
[43] M. Roman, C. Zhu, R. J. O'Malley, R. E. Gerald, and J. Huang, "Distributed fiber-optic sensing with low bending loss based on thin-core fiber," *IEEE Sensors J.*, vol. 21, no. 6, pp. 7672–7680, Mar. 2021.
[44] P. S. Westbrook *et al.*, "Enhanced optical fiber for distributed acoustic sensing beyond the limits of Rayleigh backscattering," *iScience*, vol. 23, no. 6, Jun. 2020, Art. no. 101137.

Muhammad Roman (Graduate Student Member, IEEE) received the M.S. degree in electrical engineering from the University of Engineering and Technology, Taxila, Pakistan, in 2013. He is currently pursuing the Ph.D. degree in electrical engineering with Missouri University of Science and Technology, Rolla, MO, USA.

He worked as a Lecturer in electrical engineering with the University of Wah, Rawalpindi, Pakistan, and the COMSATS Institute of Information Technology, Wah Cantt, Pakistan. He is currently working as a Graduate Research Assistant with Lightwave Technology Laboratory, Missouri University of Science and Technology. His research interests include distributed fiber-optic sensors for temperature and strain measurements in harsh environments.

Damilola Balogun was trained as a Foundry Supervisor with Nigerian Foundry Limited prior to obtaining the master's degree in metallurgical and materials engineering from the University of Lagos, Lagos, Nigeria, in 2017. He is currently pursuing the Ph.D. degree with Materials Science Department, Missouri University of Science and Technology, Rolla, MO, USA.

His research interests include peritectic behavior prediction and detection in Fe-C-Si-Mn-Al steels, and he was being advised by Dr. Ronald J. O'Malley.

Chen Zhu (Member, IEEE) received the B.E. degree in optoelectronics information engineering from Huazhong University of Science and Technology, Wuhan, China, in 2015, and the Ph.D. degree in electrical engineering from Missouri University of Science and Technology, Rolla, MO, USA, in 2021.

His research interest is focused on development of photonic, microwave, and microwave–photonic devices for sensing applications in structural health monitoring and human health.

Dr. Zhu was a recipient of the IEEE Instrumentation and Measurement Society Graduate Fellowship Award from 2018 to 2019.

Laura Bartlett is the Robert V. Wolf Endowed Professor of Metallurgical Engineering and the Foundry Educational Foundation Key Professor of Metal Casting Technology, Missouri University of Science and Technology, Rolla, MO, USA. She is the director of Robert V. Wolf Educational and Research Foundry, Missouri University of Science and Technology, and the Thermal Processing Laboratory. Her teaching and research experiences are in the areas of foundry steelmaking and physical metallurgy of iron and steel casting alloys. She has coauthored more than 40 peer-reviewed articles. Her work on development of advanced high-strength and lightweight steels for military vehicles is currently funded by the Department of Defense through organizations such as the Army Research Laboratory and Defense Logistics Agency. Some of her research interests include inclusion engineering and solidification phenomena in high-strength steels, experimental and theoretical aspects of phase transformations, microstructure–mechanical property relationships in high-strength alloys, and development of advanced high-strength and lightweight steels.

Prof. Bartlett has won several awards of distinction for her research including seven Best Paper Awards and three Research and Professional Development Awards.

Ronald J. O'Malley was a President of the Association for Iron and Steel Technology (AIST) from 2019 to 2021. He is a Lecturer for several short courses in steel manufacturing, including Brimacombe short course on Continuous Casting. He has authored more than 150 journal and conference proceedings papers, over 70 invited and contributed presentations, holds three U.S. patents. His current research focus is on H2 Ironmaking, EAF steelmaking, steel refining, clean steel processing and inclusion engineering, steel–refractory interactions, continuous casting, deformation processing, sensor development for harsh steelmaking environments, and new steel grade development.

Dr. O'Malley is serving as the Executive Board for AIST and is an AIST Distinguished Member and fellow. He is the F. Kenneth Iverson Chair Professor for Steelmaking Technologies in the Department of Metallurgical Engineering, Missouri University of Science and Technology, Rolla, MO, USA. He is also the Director of Kent D. Peaslee Steel Manufacturing Research Center (PSMRC), which is an industry-supported consortium with 18 industry members that support >$850K in research annually. He is also the PI for >$18M in research with the DOE in areas of sensors' development, hydrogen steelmaking, and electric furnace optimization. He has more than 30 years of experience in the metals' manufacturing industry at Alcoa, Armco/AK Steel, and Nucor Steel.

Rex E. Gerald II received the B.A. degree in chemistry from the University of Chicago (UC), Chicago, Illinois, and the conjoint Ph.D. degree in physical chemistry from the University of Illinois, Chicago (UIC), Chicago, and Max Planck Institute (MPI), Heidelberg, Germany.

He is a Research Professor with Lightwave Technology Laboratory of the Department of Electrical and Computer Engineering, Missouri University of Science and Technology (MS&T), Rolla, MO, USA. He holds 26 US patents and has coauthored more than 50 publications from research investigations conducted with UC, UIC, MPI, Argonne National Laboratory, and MS&T.

Jie Huang (Senior Member, IEEE) received the Ph.D. degree in electrical engineering from Clemson University, Clemson, SC, USA, in 2015.

He is the Roy A. Wilkens Endowed Associate Professor of Electrical and Computer Engineering with Missouri University of Science and Technology, Rolla, MO, USA. He established the Lightwave Technology Laboratory (LTL) with a strong track record of sustained research funding, high-quality journal publications, and state-of-the-art research infrastructure with cutting-edge capabilities. He has authored or coauthored over 100 refereed articles, 70 conference papers, one book chapter, and ten U.S. patent applications, all in the arena of advanced sensors. His research focuses on the development of optical and microwave sensors and instrumentation for applications in energy, intelligent infrastructures, clean environments, biomedical sensing, and harsh environments.